Experimental Investigation of a Flush-Walled, Diamond-Shaped Fuel Injector for High Mach Number Scramjets

Peter Michael Grossman

Thesis submitted to the faculty of the
Virginia Polytechnic Institute and State University
In partial fulfillment of the requirements for the degree of

Master of Science
In
Aerospace Engineering

J.A. Schetz, Chair
C.D. Hall
W.F. O'Brien

January 19, 2007
Blacksburg, VA

Keywords: Helium Injection, Scramjets, Penetration, Mixing, Supersonic, Hypersonic

Experimental Investigation of a Flush-Walled, Diamond-Shaped Fuel Injector for High Mach Number Scramjets

Peter Michael Grossman

(ABSTRACT)

An experimental investigation of a flush-wall, diamond-shaped injector was conducted in the Virginia Tech supersonic wind tunnel. The diamond injector was elongated in the streamwise direction and is aimed downstream angled up at 60º from the wall. Test conditions involved sonic injection of helium heated to approximately 313 K into a nominal Mach 4.0 crossstream airflow. These conditions are typical of a scramjet engine for a Mach 10 flight, and heated helium was used to safely simulate hydrogen fuel. The injector was tested at two different injectant conditions. First, it was investigated at a baseline mass flow rate of 3.4 g/s corresponding to an effective radius of 3.54 mm and a jet-to-freestream momentum flux ratio of 1.04. Second, a lower mass flow rate of 1.5 g/s corresponding to an effective ratio of 2.35 mm and a jet-to-freestream momentum flux ratio of 0.49 was studied. The diamond injector was tested both aligned with the freestream and at a 15º yaw angle for the baseline mass flow rate and aligned with the freestream at the lower mass flow rate. For comparison, round injectors angled up at 30º from the wall were also examined at both flow rates. A smaller round injector was used at the lower mass flow rate such that the jet-to-freestream momentum flux ratio was 1.75 for both cases. A concentration sampling probe and gas analyzer were used to determine the local helium concentration, while Pitot, cone-static and total temperature probes were used to determine the flow properties.

The results of the investigation can be summarized as follows. For the baseline case, the aligned diamond injector penetrated 44% higher into the crossflow than did the round injector. The addition of yaw angle increased the crossflow penetration to 53% higher than the round injector. The aligned diamond injector produced a 34% wider jet than the round injector, while the addition of yaw angle somewhat reduced this widening effect to

26% wider than the round injector. The aligned and yawed diamond injectors exhibited 10% and 15% lower mixing efficiency than the round injector, respectively. The total pressure loss parameter of the aligned diamond was 22% lower than the round injector, while the addition of yaw angle improved the total pressure loss parameter to 34% lower than the round injector. For the lower mass flow (and momentum flux ratio) case, the diamond injector demonstrated 52% higher penetration and a 39% wider plume than the round injector. The mixing efficiency was nearly identical between the two injectors with just a 4% lower mixing efficiency for the diamond injector. The total pressure loss parameter of the diamond injector was 32% lower than round injector. These results confirm the conclusions of earlier, lower free stream Mach number and higher molecular weight injectant, studies that a slender diamond injector provides significant benefits for crossflow penetration and lower total pressure losses.

List of Tables

List of Figures

Nomenclature

A = area

a, b = concentration probe calibration constants

c_p = constant pressure specific heat

c_v = constant volume specific heat

f = stoichiometric hydrogen-air ratio

G = mass flow rate

l = hotfilm active length

M = Mach number

p = (static) pressure

p_c = cone static pressure

p_t = total pressure

$p_{t,Pitot}$ = Pitot total pressure

$p_{t,rec}$ = total pressure recovery factor

$\bar{q}$ = jet-to-freestream momentum flux ratio

R = resistance and gas constant

R_b = effective radius

Re = Reynolds number

T = temperature

u = flow velocity

V = voltage

x = axial distance downstream of injector

y = lateral distance from the injector

$y^{\pm}$ = plume width

z = vertical distance from the wall

z^{+} = plume center of mass height

α = mass fraction

γ = ratio of specific heats

η = combustor efficiency

η_m = mixing efficiency

κ = hotfilm gas composition parameter

Π = total pressure loss parameter

ρ = densit

Subscripts

j = jet exit property

s = system

t = total condition

w = hot film surface

∞ = free-stream property

Table of Contents

Chapter 1 Introduction

Due to the high freestream velocity of scramjets reaching Mach 10, fuel residence time is on the order of milliseconds[1] and supersonic combustion presents an interesting challenge in scramjet engines. It is, therefore, desirable to enhance penetration and mixing of the fuel plume in order to accomplish rapid combustion. Rapid combustion will produce an increase of combustion efficiency and a reduction of the required combustor length, thus reducing the skin-friction drag and increasing the net trust. To improve the overall engine efficiency, the injection process must also induce low total pressure losses. Jet injector enhancement in high-speed flows also has applications in other fields such as thermal protection systems and vehicle control by jet thrusters.

Many injector configurations have been studied by various groups in an attempt to produce enhanced mixing and penetration in wall injectors. Some of these configurations can be seen in Figure 1.1 including swept ramps[1-10], slot injectors[11,12], transverse injection[13-18], and jet swirl[19-24]. An extensive review of injector mixing characteristics is given in Schetz et al[25]. The focus of the current investigation is single-hole, flush-walled injectors. Flush-walled injectors are preferred over in-stream injectors because they minimize total pressure losses and heating. Single-hole injectors produce a counter-rotating vortex pair[26] when they interact with the freestream crossflow. This counter-rotating vortex pair is the major method of mixing enhancement in single-hole injectors.

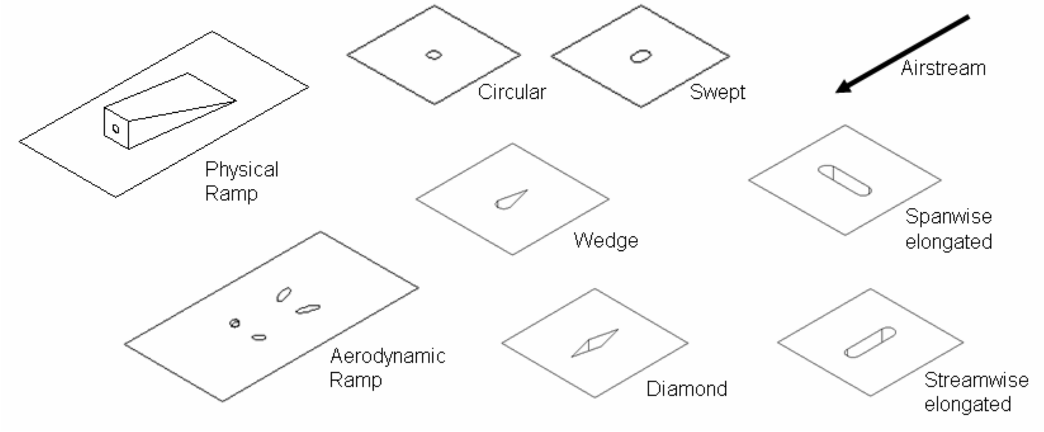

Figure 1.1: Examples of various injector configurations

One of the more successful studies in further enhancing jet flow penetration in single-hole injectors was the use of a wedge-shaped hole with a rounded back introduced by Barber et al[14]. The wedge shaped front of the hole mitigated boundary layer separation upstream of the jet resulting in higher penetration compared to round injectors. The major drawback of the wedge injector design was that separation still occurred downstream of the injector due to the rounded back. Tomioka, et al,[13] showed that replacing the round back of the injector hole with a rear facing wedge would help to negate this problem. In addition, Tomioka, et al,[13] showed that the addition of a moderate yaw angle to the diamond shaped injector further enhanced penetration and mixing. It is suggested that this phenomenon is due to the fact that the yawed diamond shape in a crossflow acts like a pitched up airfoil, thus creating suction on one side and compression on the other, inducing a span-wise flow from the compression to suction side. When this spanwise flow interacts with the counter-rotating vortex pair, streamwise vorticity is enhanced increasing penetration. Figure 1.2 shows oil flow visualizations executed at Virginia Tech demonstrating these phenomena.

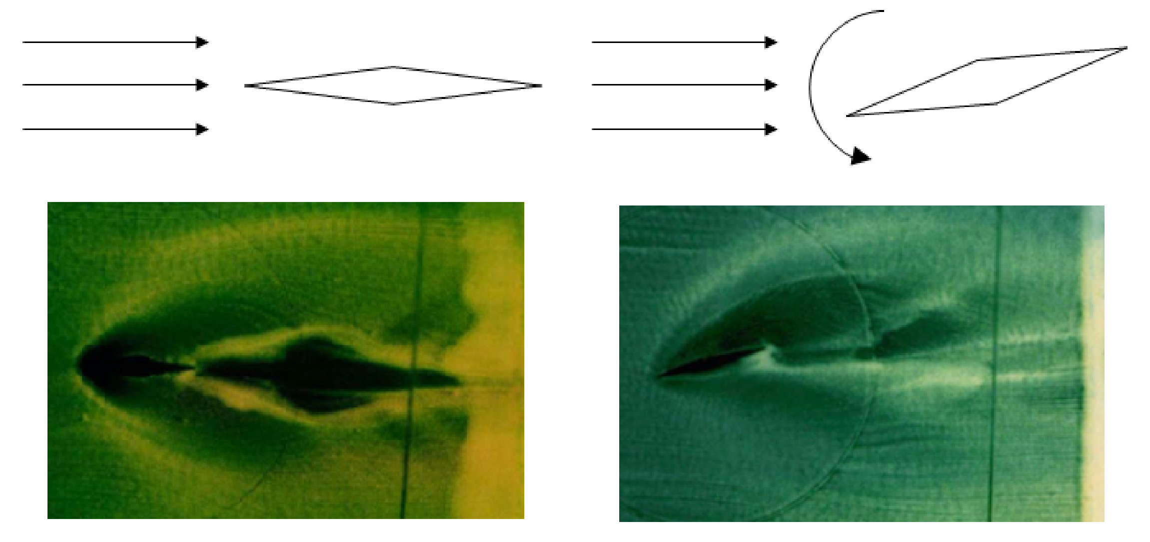

Figure 1.2: Oil flow visualizations of a diamond injector (left) aligned diamond injector (right) yawed diamond injector

The purpose of the present research is to determine the effectiveness in a nominal Mach 4.0 airflow with heated helium injectant of a diamond injector design that was initially proposed by Tomioka, et al,[13] for M = 3.0 airflow with heated air injectant. The diamond injector was tested both aligned with the free-stream flow and at a 15° yaw angle and compared to a low-angled, circular injector investigated by Maddalena et al[1] at the same nominal Mach 4.0 cross-stream conditions and mass flow rate. This comparison is intended to verify the effectiveness at nominal Mach 4.0 conditions of injector configurations that have been previously proven successful at lower Mach number conditions with simulated hydrocarbon injectants. The nominal Mach 4.0 flow simulates conditions a scramjet combustor would encounter in Mach 10 flight. Heated helium was used to safely simulate hydrogen.

Chapter 2 Test Facilities

2.1 Virginia Tech Supersonic Wind Tunnel

These experiments were conducted in the Virginia Tech supersonic wind tunnel shown in Figure 2.1. This facility is a blow-down type cold flow wind tunnel acquired from NASA Langley Research Center in 1958 and put into use at Virginia Tech in 1963. Compressed air for each run is stored in two tanks with a total capacity of 23 m^3. These tanks are pressurized by an Ingersoll-Rand Type 4-HHE-4, 4-stage reciprocating air compressor driven by a 500 hp, 480 V Marathon Electric Co. motor. The system can achieve a tank pressure of 51 atm.

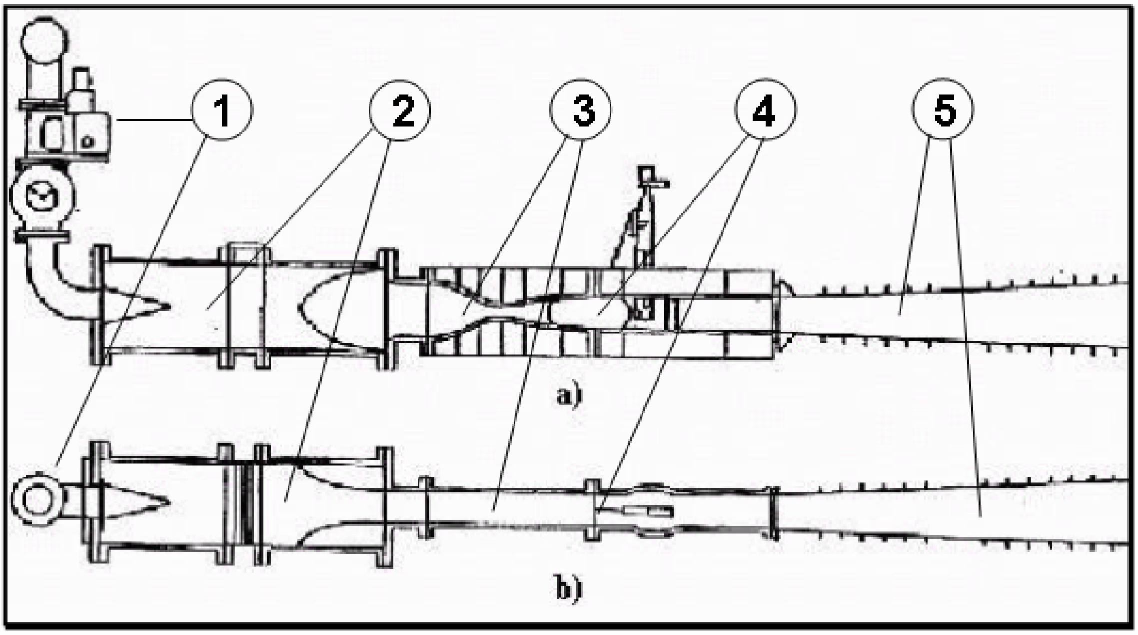

Figure 2.1: Virginia Tech Supersonic Wind Tunnel Layout

(1) – Pressure Control System (2) – Plenum Chamber (3) – Converging-Diverging Nozzle

(4) – Test Section (5) – Diffuser

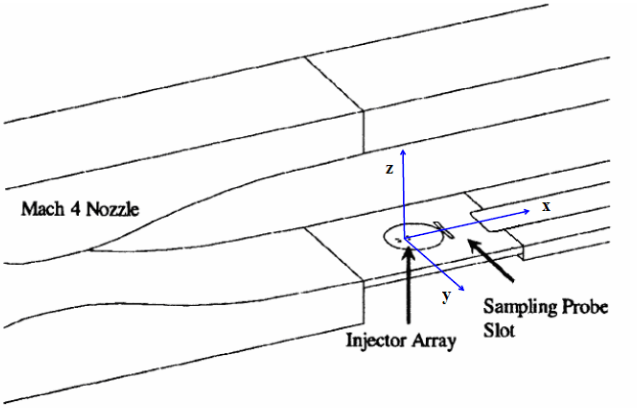

Figure 2.2: Virginia Tech supersonic wind tunnel test section experimental setup

The tunnel control system consists of a quick release butterfly valve and a 30.5 cm diameter hydraulically actuated pressure release valve with a PID feedback control to ensure the desired plenum pressure is held steady. The Virginia Tech supersonic wind tunnel setup for these experiments used a converging-diverging nozzle to achieve a nominal Mach 4 flow in the test section measuring 23 cm wide by 23 cm high and 30 cm long in the stream-wise direction. Flow conditions for these experiments involved total pressure and temperature in the plenum chamber of $P_{t,plenum}$ = 1034 kPa and $T_{t,plenum}$ = 295 K. However, there was a weak oblique shock observed at the end of the nozzle, where the floor plate attached resulting in actual freestream conditions of Mach number, M_∞ = 3.8, total pressure, $P_{t,\infty}$ = 1029 kPa and total temperature, $T_{t,\infty}$ = 295 K. Figure 2.2 shows a schematic of the wind tunnel nozzle and test section setup used in these experiments.

2.2 Data Acquisition System

Data from the experiments were acquired using a 16 channel, 16 bit A/D converter. A 64 channel multiplexer with a built in cold-junction compensator was used for temperature measurements with a sampling rate of 500 Hz. Labview was used both to control the wind tunnel, traverse system, and injection and to collect data from the measurement probes.

Chapter 3 Helium Injectors

3.1 Injection characteristics

Heated helium was used in these experiments to safely simulate hydrogen fuel in a scramjet engine. Since these experiments were concerned with plume mixing and penetration performance rather than combustion, it was unnecessary to use a combustible fuel. The helium was heated to a value of approximately 313 K by a flow heater in the feedline prior to the injector measurement devices and orifice.

When comparing injectors, it is important to normalize data to provide an objective and accurate comparison. Often, injector diameter is used to normalize lengths for round injectors of varying sizes. For injector arrays such as aeroramp injectors, equivalent diameter (the diameter of a single round injector with the same area as the total area of the injectors in the array) is employed. However, when comparing injectors of different shapes, equivalent diameter is a poor length scale because changing injection properties can affect some shapes differently from others. Thus, a different length scale must be developed. The length scale used in these experiments is the effective radius, R_b defined as follows[13]

$$R_b = \sqrt{\frac{G_j}{\rho_\infty u_\infty}} \qquad (3.1$$

where G_j is the injector mass flow, ρ_∞ is the freestream density and u_∞ is the freestream velocity.

To fully describe injector conditions, another parameter is used called the jet-to-freestream momentum flux ratio, $\bar{q}$, defined as follows

$$\overline{q} = \frac{\left(\rho u^2\right)_j}{\left(\rho u^2\right)_\infty} = \frac{\left(p\gamma M^2\right)_j}{\left(p\gamma M^2\right)_\infty} \qquad (3.2$$

where the subscript j refers to injector conditions, the subscript ∞ refers to freestream conditions, ρ is density, u is velocity, p is pressure, M is Mach number and γ is the ratio of specific heats; $\gamma = 1.4$ in the freestream (air) and 1.667 in the injector (helium).

3.2 Injector Configurations

3.21 Baseline Conditions Round Injector

The baseline case in these experiments was a round injector with a diameter of 3.226 mm angled 30° up from the wall as shown in Figure 3.1. This injector was studied by Maddalena, et al,[1] in the same facilities at the same conditions. The baseline case used a mass flow of 3.4 g/s and a jet to free stream total pressure ratio of 0.55 resulting in an effective radius of $R_b = 3.54$ mm and a jet-to-free stream momentum flux ratio of $\overline{q} = 1.75$. Values of $\overline{q}$ in this range and angled near 30° have been found to be near optimum for round injectors.[25]

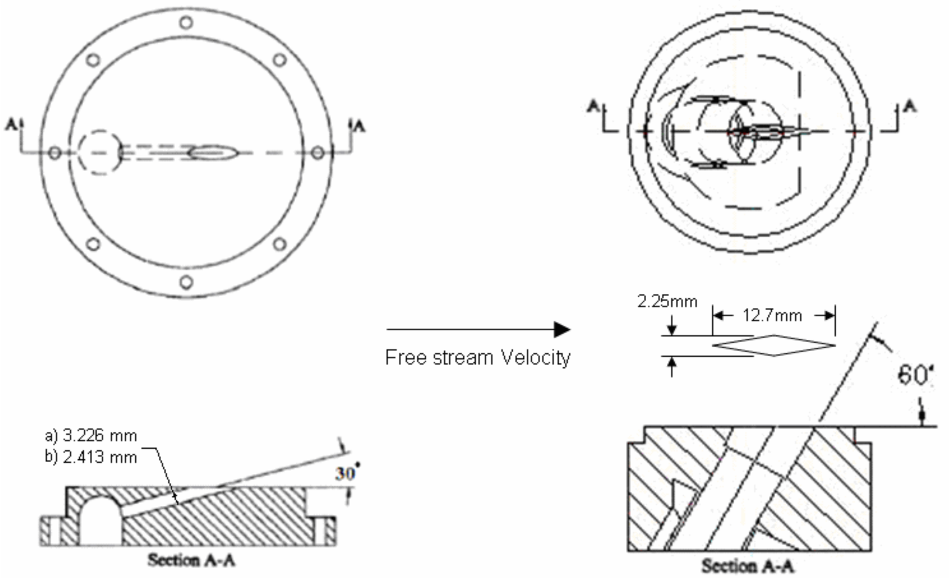

Figure 3.1: Round injector insert (left) and diamond injector insert (right)

(a) - base line case (b) - lower mass flow case

3.22 Diamond Injector

The major injector configuration studied in these experiments was the diamond shaped injector, which can be seen in Figure 3.1. The diamond had a long dimension of 12.7 mm and a short dimension of 2.25 mm and was angled 60° up from the wall (in the long direction). The 60° angle was chosen in an attempt to maximize penetration. Initially, this injector was used with flow conditions set to match the mass flow of the base case round injector of 3.4 g/s. To achieve this mass flow, the jet to free stream total pressure ratio was 0.30 resulting in an effective radius of $R_b = 3.54$ mm (matching the baseline case) and a jet-to-free stream momentum flux ratio of $\overline{q} = 1.04$. A lower $\overline{q}$ is desirable for the diamond because if $\overline{q}$ becomes too high, the jet can rapidly plume outward losing the diamond shape and its benefits.[13] The diamond baseline case was tested both with the long dimension aligned with the freestream and at a 15° yaw angle. The schlieren photograph in Figure 3.2 shows the bow shock off the front of the injector, and the injection plume can be seen.

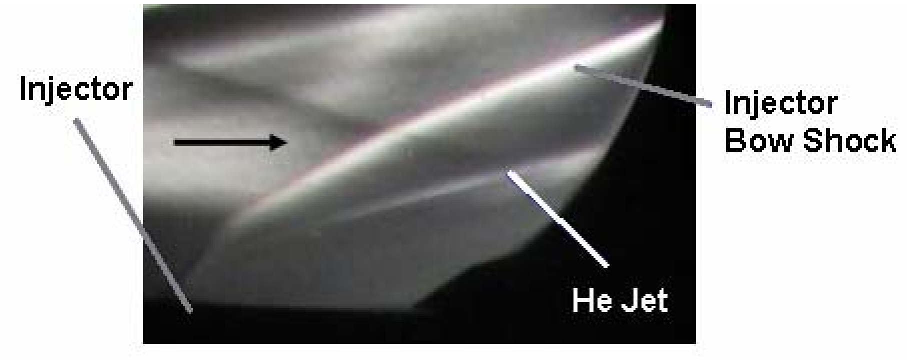

Figure 3.2: Schlieren photograph of helium injector in crossflow

The diamond injector was also tested at a lower $\overline{q}$ based on the work of Tomioka et al[13]. This research indicated that a jet-to-freestream momentum flux ratio of $\overline{q} = 0.49$ is optimal for a diamond injector of this aspect ratio[13]. To achieve this $\overline{q}$ for this diamond, a jet-to-freestream total pressure ratio of 0.13 was required resulting in a mass flow of 1.5 g/s and an effective radius of $R_b = 2.35$ mm.

3.23 Lower mass flow Round Injector

In order to provide a round injector comparison for the lower $\overline{q}$ diamond case, it was necessary to test another round injector with the same mass flow (G_j = 1.5 g/s) and effective radius (R_b = 2.35 mm) as the lower $\overline{q}$ diamond injector. To retain the same jet-to-freestream momentum flux ratio ($\overline{q}$ = 1.75) as the baseline round injector, it was necessary to create a smaller round injector with a diameter of 2.41 mm and a jet-to-freestream total pressure ratio of 0.33.

3.3 Helium Injection System

The helium injection system, shown in figure 3.3, used two bottles of compressed helium, two total pressure transducers, a differential pressure transducer, two thermocouples, and a gasline heater. One of the helium bottles was the injectant reservoir and had to be replaced every several runs. The other helium bottle was used to regulate the gasline pressure to the injector. A Victor Equipment Co. model GD-31-3837 dual pressure regulator was used to keep steady injector pressure in order to maintain a constant mass flow in the experiments. The regulator utilized a dome structure inside to maintain constant pressure. The desired pressure was input into the regulator side of the dome from the regulator helium tank. The inside of the dome was the beginning of the gasline after the reservoir bottle. With this system a steady mass flow was achieved.

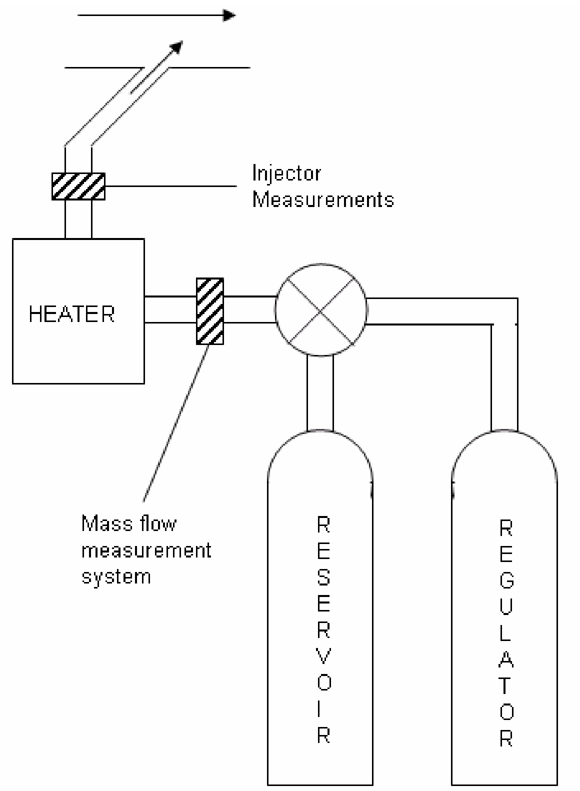

Figure 3.3: Helium injector System

The first total pressure transducer (Statham model PA822-200) and type E thermocouple with the differential pressure transducer (Lambda Square, Inc. model 150-8-16.5SA) were placed in the gasline prior to the heater in order to measure the mass flow in the gasline. The helium was then routed through the heater. The heated helium then passed the second pressure transducer (Statham model PA822-300) and a type E thermocouple in the gasline just before the injector insert to measure the injection conditions.

Chapter 4 Data Acquisition and Reduction

4.1 Test Matrix

In these experiments, injection plume measurements were taken at a vertical plane normal to the freestream flow direction 53 mm aft of the injector. This plane corresponds to a normalized distance of 15.0 R_b downstream of the baseline injectors and 22.5 R_b downstream of the lower mass flow injectors. A Cartesian coordinate system was used with its origin on the wind tunnel floor along the test section centerline. The positive x-axis was aligned with the freestream direction, the positive z-axis was in the vertical direction up from the floor and the y-axis was aligned with the tunnel span direction.

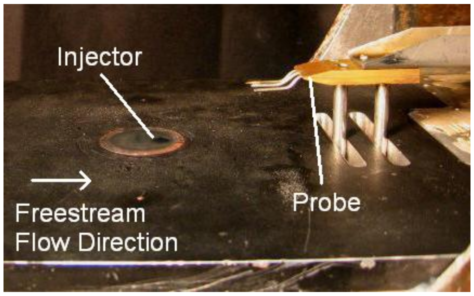

Figure 4.1: Instrument traverse system

All measurements in these experiments were accomplished using probes mounted on a vertical traversing system and inserted through slots cut in the wind tunnel floor as shown in Figure 4.1. This system traveled 28 mm vertically in 32 steps at a speed of 900 steps per second at a velocity of 4.4 mm/s driven by a Rapid Sym model 34D-9209A stepper motor. The probe was held at each step position for 300 ms to allow the measurements to come to a steady state. The sampling rate of 500 Hz resulted in a total of 150 samples from each measurement position. Data at each position were calculated from the average of the last 25 samples at that step. This setup was used to acquire data for a single vertical profile for each probe for one wind tunnel run. Between runs, the probe spanwise position was adjusted manually. To produce a full profile at the measurement plane, a vertical profile was taken at each of 13, equally-spaced spanwise stations over a distance of 38 mm. The uncertainty in the probe position was ±0.3 mm in the spanwise direction and ±0.2 mm in the vertical direction.

4.2 Instrumentation

4.2.1 Species Composition probing

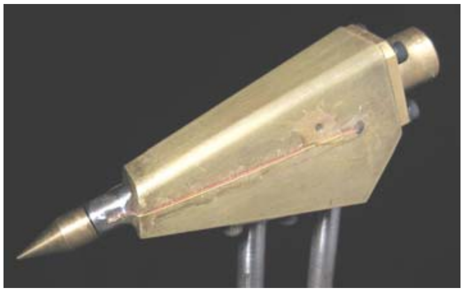

Figure 4.2: Helium Concentration Probe

Mean helium concentration measurements were accomplished using the integrated concentration sampling probe and gas analyzer designed for supersonic flow shown in Figure 4.2. The probe was aspirated during data acquisition by a vacuum pump. Measurements were obtained following a divergent section of an internal channel in the probe with a choked exit. The choked exit and inlet orifice of the probe both had a diameter of 0.63 mm which was designed to prevent the formation of a standoff shock at the inlet. The measurement plane channel diameter was 3.8 mm. The hotfilm in the probe had a diameter of 50.8 μm and an active sensor length of 1.02 mm. The conceptual design of this type of probe was originally developed by Ng et al[27]. The concentration probe was calibrated to measure a unique helium mass fraction for a specific pressure, temperature and heat transfer rate at the hotfilm sensor plane.

The hotfilm voltage was related to the hotfilm Reynolds number by

$$V^2 = \frac{(R_s - R_w)^2}{R_w} \pi l \kappa \left(a \,\mathrm{Re}^b\right)\left(T_w - T_t\right) \tag{4.1}$$

Where Re is the hotfilm Reynolds number, R_s, R_w, l and T_w are hot film quantities which are known, κ is a function of the gas composition and T_t is the total temperature measured by a thermocouple at the sensor location. The values, a and b, are calibration constants found empirically using the following relation using several data points at each calibration level.

$$Nu = a \,\mathrm{Re}^b \tag{4.2}$$

where Nu is the hotfilm Nusselt number.

A file was generated showing the probe position, voltage, total pressure and total temperature for each wind tunnel run. For each probe position, a computer algorithm using these measurements with equation 4.1 was used to determine the upper and lower bounds on voltage for any calibration level. The program then searched iteratively for the two helium concentration calibration curves which bounded the voltage at the measured pressure and temperature. Then, the local helium concentration was interpolated between the two bounding curves. These algorithms are shown in Appendix A.1. The probe was found to have an uncertainty of approximately ±3% for helium mass fraction measurements.

4.2.2 Aerothermodynamic probing

Figure 4.3: Aero-Thermodynamic triple rake probe (top) Pitot Probe (middle) Total Temperature Probe (bottom) Cone-Static Probe

Aerothermodynamic measurements were taken with a triple-rake probe which included a Pitot pressure probe, a cone-static pressure probe and a total temperature probe as seen in Figure 4.3. The Pitot probe had an outer diameter of 1.59 mm and an inner diameter of 1.04 mm. The Pitot probe capture area was 0.85 mm^2. The cone-static probe used the same size tubing as the Pitot probe, but was capped with a 10º half-angle cone with four small ports around its surface to reduce misalignment effects with respect to the flow.

These measurements along with the helium concentration were used with a combination of the Rayleigh-Pitot formula and a numerical solution of the Taylor-Maccoll equation to determine the local Mach number and total pressure at each sampling location. The Rayleigh-Pitot formula assumes a normal shock at the Pitot probe inlet and provides the ratio of local total pressure to Pitot pressure as a function of Mach number

$$\frac{P_t}{P_{t,2}} = f(M,\gamma). \qquad (4.3$$

The Taylor-Maccoll solution provides a ratio of the cone-static surface pressure to the local total pressure as a function of Mach number

$$\frac{P_c}{P_t} = f(M,\gamma). \qquad (4.4$$

Equations 4.3 and 4.4 can be combined to provide a ratio of cone-static pressure to Pitot pressure as a function of Mach number

$$\frac{P_c}{P_{t,2}} = f(M,\gamma). \qquad (4.5$$

Once the Mach number is found, the local total pressure can then be calculated using the Rayleigh-Pitot normal shock relation

$$P_t = P_{t,2}\left(\left(\frac{(\gamma+1)M^2}{(\gamma-1)M^2+2}\right)^{\frac{\gamma}{\gamma-1}}\left(\frac{\gamma+1}{2\gamma M^2-(\gamma-1)}\right)^{\frac{1}{\gamma-1}}\right)^{-1}. \qquad (4.6$$

Where the local Mach number is between 1.0 and 1.1, the static pressure ratio, $P/P_{t,\infty}$ (from isentropic flow relations) is constant and equal to that found at Mach 1.1 using equation 4.5. the local static pressure at any point in this inner supersonic region can be found by simply multiplying this ratio by the Pitot pressure. Once the Pitot pressure and static pressure are known, the Mach number and local total pressure can be determined using the isentropic flow relations and equation 4.6. If the local Mach number becomes subsonic, the Pitot pressure measured is simply equal to the local total pressure.

The uncertainty on the pressure measurements was ±6 kPa. The Algorithms used to complete these calculations can be found in full in appendix A.2. All other flow properties were then found using the perfect gas relations. All calculations assumed a calorically perfect gas, i.e. constant specific heats.

The total temperature was measured directly by the total temperature probe because total temperature remains constant across a normal shock. The uncertainty on the temperature measurements was ±2 K.

Chapter 5 Results and Analysis

5.1 Baseline Cases

This section discusses the total temperature, total pressure and concentration (mass fraction) data for the injectors using a mass flow of G_j = 3.4 g/s corresponding to an effective radius, R_b, of 3.54 mm. The results for the aligned and yawed diamond were compared to the baseline round injector. All plots in this section were taken from the measurement plane 15.0 R_b downstream of the injectors. The plots extend to $\pm$5.35 R_b in the spanwise direction and from 0 to 7.65 R_b in the vertical direction.

5.1.1 Total Temperature Contours

Figure 5.1 shows the total temperature contours for the baseline mass flow cases. These figures represent the results for aero-thermodynamic measurements by the total temperature probe. The local total temperature values in the plots are normalized by the freestream total temperature of approximately $T_{t,\infty}$ = 295 K. All three profiles are set to the same non-dimensional scale for comparison. A qualitative and somewhat quantitative assessment of the injector behaviors can be obtained from the isothermal profiles.

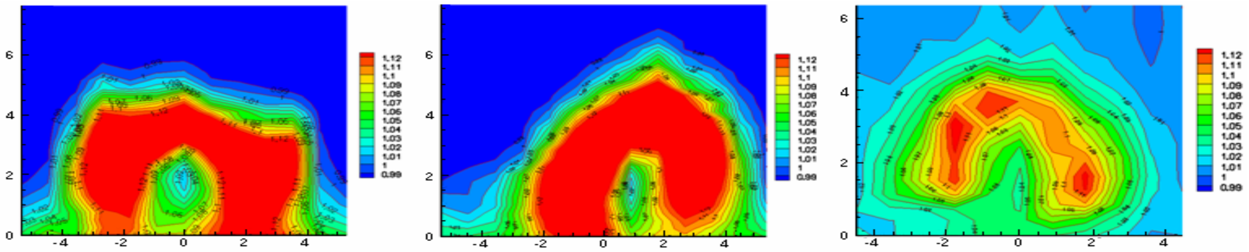

Figure 5.1: Normalized total temperature contours, $T_t/T_{t,\infty}$, for baseline case (left) aligned diamond injector (middle) yawed diamond injector (right) round injector

The total temperature profiles for all three injector configurations show an arch-shaped structure which is often demonstrative of the presence of a counter-rotating vortex pair. The counter-rotating vortex pair is present in most single-hole injectors in a supersonic crossflow. The vortex pair is the main mechanism for mixing enhancement and penetration for single-hole injectors.

The total temperature contours show a cooler core, a warmer exterior and a more gradual temperature gradient in the round injector than the diamond injectors, which display a well-bounded hot core with a rapid drop off to the freestream total temperature at the edge of the arch structures. This observation would indicate that the circular injector generates better mixing than the diamond injectors. However, it is often misleading to use a temperature mixing analogy due to the Ranque-Hilsch effect. This effect states that total temperature is variable within a vortex structure, rendering the temperature analogy for mixing inconclusive.

5.1.2 Total Pressure Contours and Total Pressure Loss Parameter

Figure 5.2 shows the total pressure contours for the baseline mass flow cases. These contours represent the results of the aero-thermodynamic measurements using equations 4.5 and 4.6. The local total pressure values in the plots are normalized by the freestream total pressure of approximately $P_{t,\infty}$ = 1029 kPa. All three profiles are set to the same non-dimensional scale for comparison. A qualitative and quantitative assessment of the injector behaviors can be obtained from the isobaric profiles which show the local total pressure losses. Pressure losses from the air and fuel can be generated by viscous forces in the boundary layer, flow separation, shock waves, or fuel –air mixing.

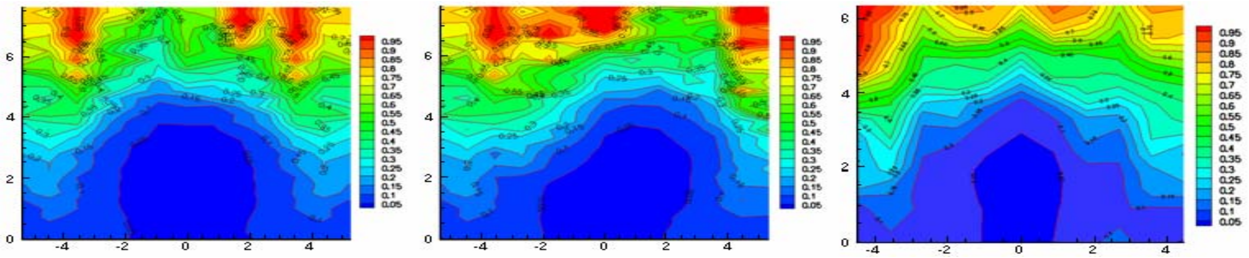

Figure 5.2: Normalized total pressure contours, $P_t/P_{t,\infty}$, for baseline cases (left) aligned diamond injector (middle) yawed diamond injector (right) round injector

The total pressure profiles indicate that the diamond injectors generate slightly higher local total pressure losses over a larger area than the round injector. However, the overall average total pressure losses are more revealing for injector performance than local observations. The overall total pressure loss is quantified using a total pressure loss parameter calculated using a numerical integration of the mass flow weighted total pressure field over the sampling plane. The total pressure loss parameter, Π, is related to the pressure recovery factor, $p_{t,rec}$, as follows[1]

$$p_{t,rec} = \frac{\int \rho u p_t dA}{\rho_j u_j p_{t,j} A_j + \int \rho_\infty u_\infty p_{t,\infty} dA} \qquad (5.1$$

and

$$\Pi = 1 - p_{t,rec} \qquad (5.2$$

where ρ is density, u is velocity, p_t is local total pressure, and A is area. In equation 5.1, the numerator represents the local properties at the measurement plane, the subscript j refers to jet (injector) properties and the subscript ∞ refers to free stream properties. Density and velocity were obtained using the ideal gas relations.

For equation 5.2, a total pressure loss parameter value of $\Pi = 0$ indicates no overall total pressure loss. The results of the total pressure loss parameter calculations can be seen in Table 5.1. These results state that the diamond injectors generate lower overall pressure losses than the round injector. The aligned diamond shows a total pressure loss parameter of $\Pi = 0.294$ as compared to the round injector total pressure loss parameter of $\Pi = 0.378$, while the yawed diamond injector shows further improvement with a total pressure loss parameter of $\Pi = 0.250$. The diamond injectors generate lower overall total pressure losses despite showing higher local pressure losses, because overall total pressure loss is mass flow averaged. Thus it is a function not only of local pressure but also of density and velocity. The round injector generates a higher velocity field near the jet plume than the diamond injectors, because it uses the same mass flow for similar density through a smaller hole.

5.1.3 Mass Fraction Contours and Jet Interaction parameters

Figure 5.3 shows helium mass fraction contours representing the results of the concentration measurements. The magnitude of maximum helium concentration, α_{max}, is identified on each plot and its location is designated by a **x** symbol. The minimum isoline, $\alpha = 0.028$, represents the stoichiometric value for homogeneous H_2-air combustion at ambient conditions. The centroid of the lean limit mass fraction ($\alpha = 0.003$)[1] is considered the plume center of mass and is marked by a ▪ symbol in the plots.

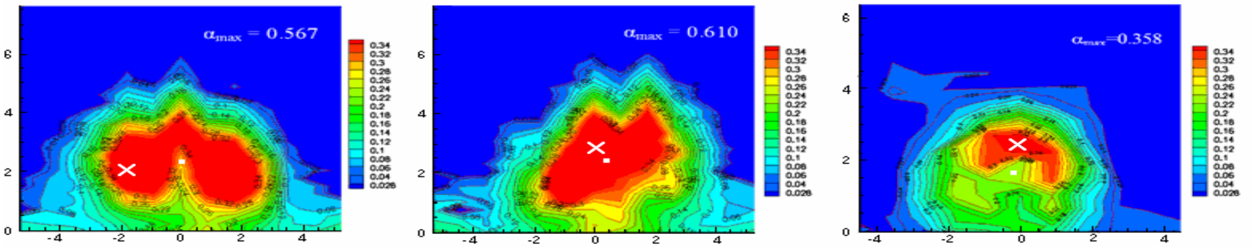

Figure 5.3: Mass fraction contours, α, for baseline cases
(left) aligned diamond injector (middle) yawed diamond injector (right) round injector

The mass fraction contours show that the core of the jet, defined as the location of maximum concentration is located at (y/R_b, z/R_b) = (-1.79, 2.07) for the aligned diamond injector, (y/R_b, z/R_b) = (0.00, 2.84) for the yawed diamond injector, and (y/R_b, z/R_b) = (0.00, 2.48) for the round injector. The jet core for all three injectors is within the boundary layer which has a thickness of 5.65 R_b at the measurement plane.

Figure 5.3 indicates that the diamond injectors produce a larger spread of helium with higher penetration while the round injector generates more mixing. The two diamond injectors show similar mixing performance while the yawed diamond injector plume is narrower but with higher penetration. The characteristic dual-lobe structure indicating a counter-rotating vortex pair is evident in the aligned diamond injector and the round injector, but for the yawed diamond injector, the cores are not obvious. Figure 5.4 shows the two diamond injector mass fraction contours with a larger range of mass fraction isolines to capture the internal structure of the plume core. With the expanded range, the two cores of the vortex pair become visible in the yawed diamond, but one is higher than the other and they are no longer side by side. This phenomenon is likely due to the addition of spanwise flow generated by the yawed diamond shape. The interaction of the spanwise flow with the vortex pair enhances streamwise vorticity, thus increasing jet penetration.

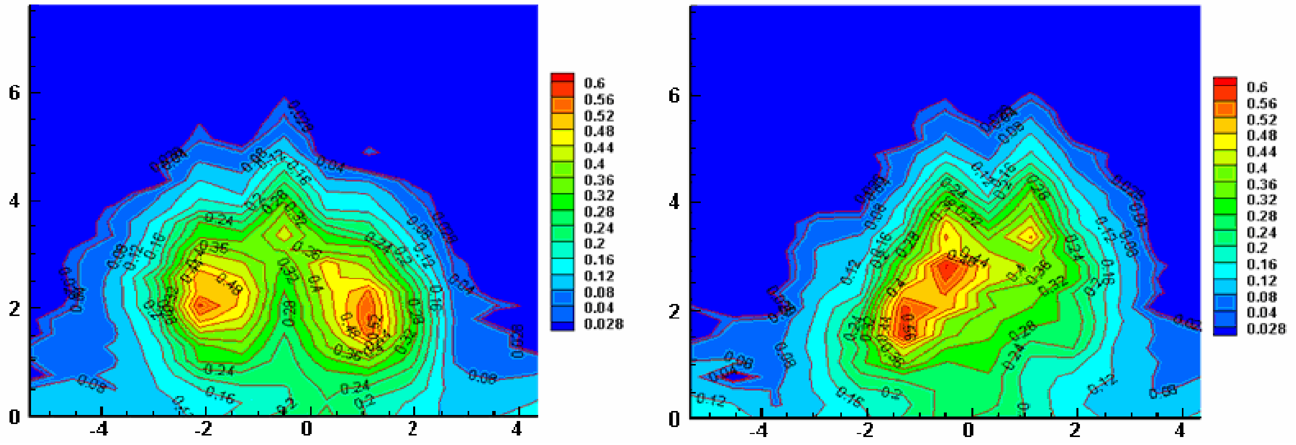

Figure 5.4: Mass fraction contours, α, with expanded range
(left) aligned diamond injector (right) yawed diamond injector

To quantify injector penetration performance, the z-coordinate of the plume center of mass is used. This indicates the penetration of the plume into the supersonic crossflow[1]

$$z^{+} = \frac{\int \rho u \alpha z dA}{\int \rho u \alpha dA} \qquad \text{(5.3}$$

where ρ is the local density, u is the local velocity, α is the local helium mass fraction, z is the normalized distance above the tunnel floor and dA is the differential area. These integrals were evaluated numerically and the results can be found in Table 5.1 which shows that aligned diamond injector penetrates to a height of $z^{+} = 2.30\ R_b$, which is higher than the round injector penetration of $z^{+} = 1.60\ R_b$. The yawed diamond injector penetrates slightly higher still to a height of $z^{+} = 2.44\ R_b$. Plume width performance, $y^{\pm}$, is also presented in table 5.1. The plume width is defined as the normalized spanwise distance between the stoichiometric edges of the plume. Both diamond injectors generate wider plumes than the round injector which spread to a width of $y^{\pm} = 6.3\ R_b$. The aligned diamond injector plume is slightly wider with a width of $y^{\pm} = 8.5\ R_b$ than the yawed diamond injector which had a width of $y^{\pm} = 8.0\ R_b$.

Since there is no combustion occurring in this non-reacting simulation, it is useful to quantify the mixing performance of the injector to predict the combustion performance in an actual supersonic combustor with the same pressure field. The mixing performance is quantified by a mixing efficiency value, η_m, defined by the mass flow rate fuel which would theoretically react assuming quasi 1-dimensional, steady isentropic flow over the total mass flow rate of the fuel as follows[1]

$$\eta_m = \frac{\int \rho u Z dA}{\int \rho u \alpha dA} \qquad (5.4$$

where Z is a stoichiometric evaluation of mass fraction as follows

$$\begin{aligned} Z &= \alpha \ \text{ if } \ \alpha \le f \\ Z &= \frac{(1-\alpha)f}{(1-f)} \ \text{ if } \ \alpha > f \end{aligned} \qquad (5.5$$

where f is the stoichiometric combustion mass fraction value ($\alpha = 0.028$). In equation 5.5, $\alpha \le f$ represents the H_2 lean to H_2 consumed case and $\alpha > f$ represents the O_2 lean to O_2 consumed case. Mixing efficiencies are shown in Table 5.1. The aligned and yawed diamond injectors have similar mixing efficiency values of 0.18 and 0.17 respectively. While the round injector mixes slightly faster with an efficiency value of 0.20.

Table 5.1 displays all the injector performance parameters for the baseline cases at a measurement plane 15.0 R_b downstream of the injector orifices. Both diamond injectors show better penetration than the round injector. The aligned diamond injector penetrated 44% higher than the round injector while the yawed diamond penetrated 53% higher than the round injector. The diamond injectors produce not only higher penetrating plumes, but also wider plumes compared to the round injector. The aligned diamond injector produced a plume 34% wider than the round injector while the yawed diamond injector produced a 26% wider plume than the round injector.

Table 5.1: Baseline Injectors plume parameters

Parameter	Aligned Diamond Injector	Yawed Diamond Injector	Round Injector
z^+	2.30	2.44	1.60
η_m	0.18	0.17	0.20
Π	0.294	0.250	0.378
$y^\pm$	8.5	8.0	6.3

The mixing efficiencies are nearly identical between the two diamond injectors and both mix 10% – 15% slower than the round injector as qualitatively expected from Figure 5.3. The results in Table 5.1 also show that the diamond injectors generate lower overall pressure losses than the round injector. The aligned diamond injector generates 22% lower total pressure loss than the round injector, while the yawed diamond injector generates 34% lower total pressure loss than the round injector.

5.2 Lower Mass Flow cases

This section discusses the total temperature, total pressure and concentration (mass fraction) data for the injectors using a mass flow of G_j = 1.5 g/s corresponding to an effective radius of 2.57 mm. The results for the lower $\overline{q}$ ($\overline{q}$ = 0.49) diamond were compared to the lower R_b round injector ($\overline{q}$ = 1.75). These conditions correspond to a “well-designed” round injector compared to a “well-designed” diamond injector. All plots in this section were taken from the measurement plane 22.5 R_b downstream of the injectors. The plots extend to $\pm$5.35 R_b in the spanwise direction and from 0 to 7.65 R_b in the vertical direction.

5.2.1 Total Temperature Contours

Figure 5.5 shows the total temperature contours for the lower mass flow cases. These figures represent the results for aero-thermodynamic measurements by the total temperature probe. The local total temperature values in the plots are normalized by the freestream total temperature of approximately $T_{t,\infty}$ = 295 K. Both profiles are set to the same non-dimensional scale for comparison. An assessment of the injector behaviors can be obtained from the isothermal profiles.

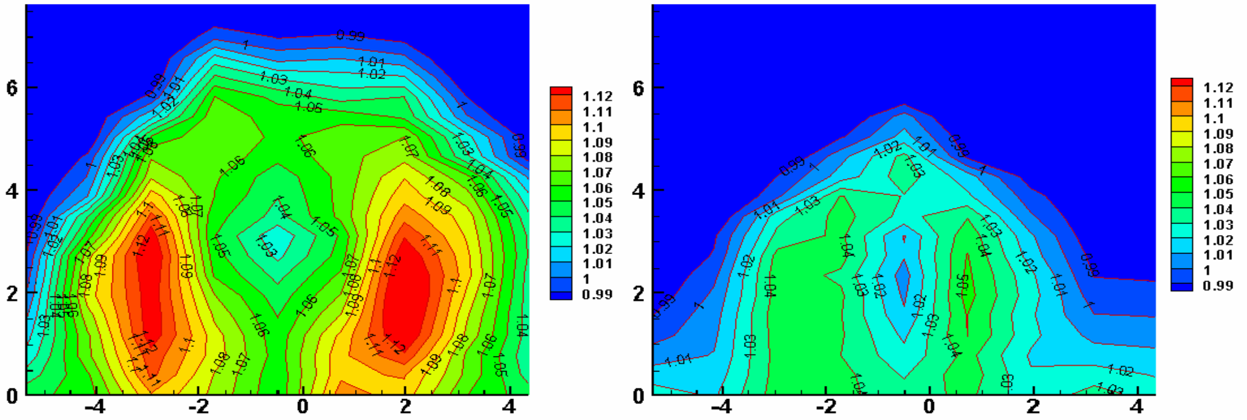

Figure 5.5: Normalized total temperature contours, $T_t/T_{t,\infty}$, for lower mass flow cases (left) diamond injector (right) round injector

Both injector configurations total temperature profiles show the dual-lobe structure seen in the baseline cases which is indicative of the presence of a counter-rotating vortex pair. The total temperature contour shows a temperature gradient in the round injector profile with lower maximum temperature than the diamond injector .The diamond injector higher temperature lobes indicate that more helium was trapped in the vortex cores. This observation is based on the fact that the helium is heated while the free stream air is cold, thus, areas of higher temperature are observed to contain more heated helium. This observation would indicate that the circular injector generates better mixing than the diamond injector. However, as previously discussed, it is often misleading to use a temperature mixing analogy due to the Ranque-Hilsch effect.

5.2.2 Total Pressure Contours and Total Pressure Loss Parameter

Figure 5.6 shows the total pressure contours for the lower mass flow cases. These contours represent the results of the aero-thermodynamic measurements using equations 4.5 and 4.6. The local total pressure values in the plots are normalized by the freestream total pressure of approximately $P_{t,\infty}$ = 1029 kPa. Both profiles are set to the same non-dimensional scale for comparison.

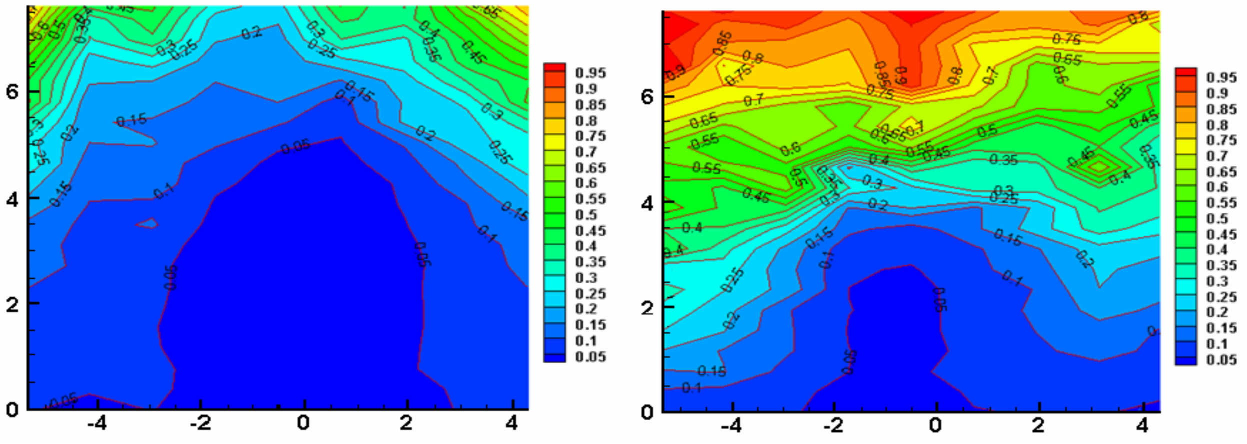

Figure 5.6: Normalized total pressure contours, Pt/Pt,∞ , for lower mass flow cases (left) diamond injector (right) round injector

The total pressure profiles indicate that the diamond injectors generate total pressure losses over a larger area than the round injector. However, the overall average total pressure losses are more revealing for injector performance than local observations. The overall total pressure loss is quantified using the previously discussed total pressure loss parameter calculate using a numerical integration of the mass flow weighted total pressure field over the sampling plane.

The results of the total pressure loss parameter calculations can be seen in Table 5.2. These results indicate that the diamond injector generates lower overall total pressure loss than the round injector. The diamond injector shows a total pressure loss parameter of $\Pi = 0.253$ as compared to the round injector which shows a total pressure loss parameter of $\Pi = 0.373$.

5.2.3 Mass Fraction Contours and Jet Interaction parameters

Figure 5.7 shows helium mass fraction contours representing the results of the concentration measurements for the lower mass flow case. The magnitude of maximum helium concentration, α_{max} is identified on each plot and its location is designated by an **x** symbol. The minimum isoline, $\alpha = 0.028$, represents the stoichiometric value of mass fraction for homogeneous H_2-air combustion at ambient conditions. The centroid of the lean limit mass fracation ($\alpha = 0.003$)[1] is considered the plume center of mass and is marked by a ▪ symbol in the plots.

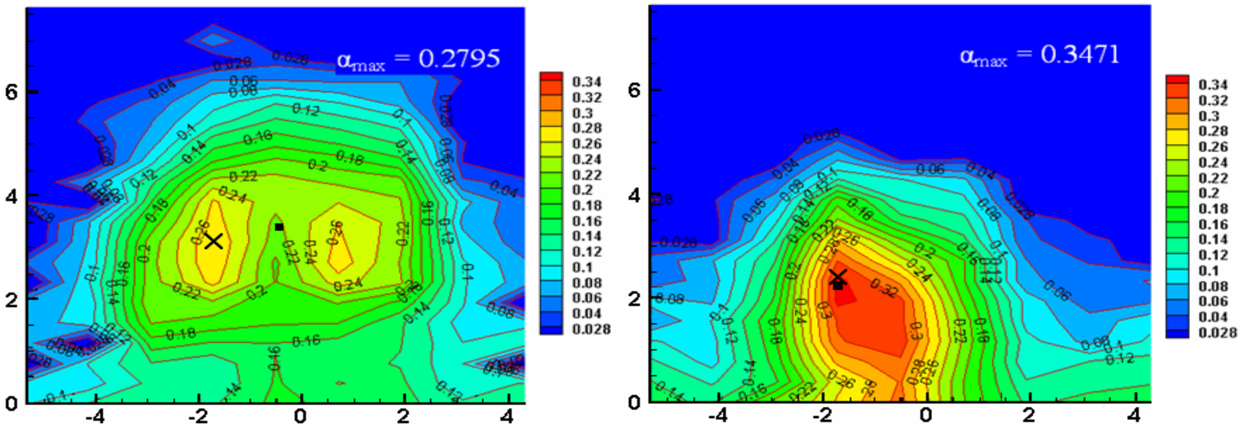

Figure 5.7: Mass fraction contours, α, for lower mass flow cases (left) diamond injector (right) round injector

The mass fraction contours show that the core of the jet, defined as the location of maximum concentration is located at (y/R_b, z/R_b) = (-1.36, 3.12) for the diamond injector and (y/R_b, z/R_b) = (-1.36, 2.33) for the round injector. The jet core for both injectors is within the boundary layer which has a thickness of 8.50 R_b at the measurement plane.

Figure 5.7 indicates that the diamond injector produces a larger spread of helium with higher penetration than the round injector. The characteristic dual-lobe structure indicating the presence of the counter-rotating vortex pair is evident in the diamond injector profile, while the two cores have merged by the measurement plane in the round injector.

To quantify injector penetration performance, the z-coordinate of the plume center of mass is used. Equation 5.3 was used as before to determine the plume penetration, z^+. The results can be found in Table 5.2 which shows that the diamond injector penetrates to a height of $z^+ = 3.37\ R_b$, which is higher than the round injector penetration height of $z^+ = 2.22\ R_b$. Plume width performance, $y^{\pm}$, is also presented in Table 5.2. The plume width is defined as before as the normalized spanwise distance between the stoichiometric edges of the plume. The diamond injector generates a wider plume with a width of $y^{\pm} = 10.5\ R_b$ than the round injector with a plume width of $y^{\pm} = 7.5\ R_b$.

The mixing performance is quantified as before by a mixing efficiency value, η_m, defined by the mass flow rate fuel which would theoretically react assuming quasi 1-dimensional, steady isentropic flow over the total mass flow rate of the fuel using equation 5.4 as previously described. These efficiencies are displayed in Table 5.2 which shows that the diamond and round injectors have similar mixing efficiency values of 0.26 and 0.27, respectively.

Table 5.2 displays all the injector performance parameters for the lower mass flow injectors at a measurement plane 22.5 R_b downstream of the injector orifices. The diamond injector shows better penetration than the round injector. The aligned diamond injector penetrated 52% higher than the round injector. The diamond injector produces not only an higher penetrating plume, but also a wider plume compared to the round injector. The diamond injector produced a plume 39% wider than the round injector.

The mixing efficiencies are nearly identical between the two injectors with the diamond injector mixing just 4% slower than the round injector. The results presented in Table 5.2 also state that the diamond injector generates lower overall total pressure loss than the round injector. The diamond injector generates 32% lower total pressure loss than the round injector for the lower mass flow case.

Table 5.2: Lower mass flow injectors plume parameters

Parameter	Diamond Injector	Round Injector
z^+	3.37	2.22
η_m	0.26	0.27
Π	0.253	0.373
$y^{\pm}$	10.5	7.5

5.3 Injector comparison

The baseline injectors and lower mass flow injectors cannot be compared directly due to the different normalized measurement planes and R_b values. However, the percent performance improvement over the equivalent round injector can be compared for each diamond configuration as shown in Table 5.3.

Table 5.3: Percent improvement of Diamond injectors over round injectors

Parameter	Aligned Diamond Injector ($\overline{q}$ = 1.2)	Yawed Diamond Injector ($\overline{q}$ = 1.2)	Lower mass flow Diamond Injector ($\overline{q}$ = 0.5)
z^+	44 %	53 %	52 %
η_m	- 10 %	- 15 %	- 4 %
Π	22 %	34 %	32 %
$y^{\pm}$	34 %	26 %	39 %

Table 5.3 shows that the lower mass flow (lower $\overline{q}$) diamond injector combines the advantages of the aligned and yawed baseline injectors. The lower mass flow diamond injector generates the higher penetration and improved total pressure loss of the yawed baseline diamond injector while generating an even wider plume as compared to the round injector than the aligned baseline injector. The lower mass flow diamond injector also generates a mixing efficiency which is closer to the round injector than the baseline mass flow cases.

Chapter 6 Summary and Conclusions

Experiments were conducted at Virginia Tech to evaluate the performance of different flush-walled fuel injectors for use in scramjet engines. The study focused on 60º diamond injectors; 30º round injectors were also tested for comparison. The diamond injector was investigated both aligned with the freestream flow and at a yaw angle of 15º at the baseline mass flow of G_j = 3.4 g/s corresponding to an effective radius of R_b = 3.54 mm and a jet-to-freestream momentum flux ratio of $\overline{q}$ = 1.04. The diamond injector was also investigated aligned with the freestream flow at the lower mass flow case of G_j = 1.5 g/s corresponding to an effective radius of R_b = 2.35 mm in order to test the lower jet-to-free stream momentum flux ratio of $\overline{q}$ = 0.49 shown to be optimal at other conditions[13]. The round injector investigated at the lower mass flow condition had a smaller actual diameter than the round injector at the baseline mass flow in order to keep the same jet-to-free stream momentum flux ratio of $\overline{q}$ = 1.75 for both cases.

Helium was used as the injectant to safely simulate hydrogen fuel for real scramjet operation. The investigation was conducted in the Virginia Tech supersonic wind tunnel with a nominal Mach 4 nozzle to simulate the Mach number seen in the combustor of a scramjet flying at Mach 10. For these experiments, there was a weak oblique shock at the end of the nozzle resulting in a Mach number of M_∞ = 3.8, total pressure of $P_{t,\infty}$ = 1029 kPa and total temperature of $T_{t,\infty}$ = 295 K in the freestream.

Profiles of total temperature, total pressure and helium concentration were generated at measurement planes normal to the freestream flow to qualitatively evaluate the injector performance. The measurement plane was 15.0 R_b downstream of the injectors for the baseline case and 22.5 R_b downstream of the injectors for the lower mass flow case. For quantitative evaluation of injector performance, several performance parameters were used: normalized jet penetration, mixing efficiency, total pressure loss parameter, and normalized plume width.

Conclusions from the investigation can be summarized as follows. For the baseline cases, the aligned diamond injector showed 44% higher penetration than the round injector while yawing the diamond injector improved penetration to 53% higher than the round injector. The aligned and yawed diamond injectors generated similar mixing efficiencies that were 10% and 15% lower than the round injector, respectively. Yawing the diamond injector also improved the total pressure loss parameter producing a value 34% lower than the round injector as compared to a value 22% lower than the round injector for the aligned diamond injector. The yaw angle was a detriment to the plume width as the aligned diamond injector produced a 34% wider plume than the round injector while the yawed diamond only produced a 22% wider plume than the round injector.

For the lower mass flow case, the diamond injector showed similar performance to the baseline yawed diamond injector when compared to their respective round injectors showing a 53% penetration increase. The lower mass flow diamond injector improved to nearly the same mixing efficiency as the round injector with just a 4% lower value. The lower mass flow diamond injector showed similar total pressure loss to the baseline yawed diamond injector with a total pressure loss parameter 32% lower than the round injector. The lower mass flow showed improved plume width over both the baseline diamond injectors with a 39% wider plume than the round injector. The lower mass flow cases were selected to compare a "well-designed" diamond injector to a "well-designed" round injector. These conclusions were found to be nominally similar to the results found by Tomioka, et al,[13] with heated air in a Mach 3.0 crossflow.

Further investigations of the diamond injectors could include the following. A yawed case at the lower mass flow conditions could be conducted to determine if the same trends hold as in the baseline case. The measurement plane could be shifted forward and aft in both cases to investigate how the plumes develop as they move downstream of the injector. Finally, testing at hot-flow freestream conditions could be investigated to simulate the flow in a real scramjet case.

References

1. Maddalena, L., Campioli, T.L., Schetz, J.A., "Experimental and Computational Investigation of an Aeroramp Injector in a Mach Four Cross Flow," AIAA/CIRA 13th International Space Planes and Hypersonics Systems and Technologies, AIAA 2005-3235, June 2005.

2. Hartfield, R.J., Hollo, S.D., and McDaniel, J.C., "Experimental Investigations of a Supersonic Swept Ramp Injector using Laser Induced Iodine Fluorescence," Journal of propulsion and power, Vol.10 No.1,1994, pp. 129-135, January-February.

3. Doerner S.E., Cutler A.D., "Effects of Jet Swirl on Mixing of a Light Gas Jet in a Supersonic Airstream," NASA/CR-1999-209842, December 1999

4. Schetz J.A., Cox-Stouffer S., Fuller R., "Integrated CFD and Experimental Studies of Complex Injectors in Supersonic Flows," AIAA 98-2780, June 1998

5. Jacobsen L.S., Gallimore S.D., Schetz J.A., O'Brien W.F., "Integration of an Aeroramp Injector/Plasma Igniter for Hydrocarbon Scramjets," Journal of Propulsion and Power Vol. 19, No. 2, March-April 2003

6. Fuller R.P., Wu P.K., Nejad A.S., Schetz J.A., "Comparison of Physical and Aerodynamic Ramps as Fuel Injectors in Supersonic Flow," Journal of Propulsion and Power, Vol. 14, No. 2, March-April 1998

7. Jacobsen L.S., Gallimore S.D., Schetz J.A., O'Brien W.F., Goss L.P., "Improved Aerodynamic-Ramp Injector in Supersonic Flow," Journal of Propulsion and Power, Vol. 19, No. 4, July-August 2003

8. Viti V., Schetz J.A., Neel R., "Numerical Studies of the Jet Interaction Flowfield with a Main Jet and an Array of Smaller Jets," ICAS 2002-4.7.1

9. Schetz J.A., Cox-Stouffer S., Fuller R., "Integrated CFD and Experimental Studies of Complex Injectors in Supersonic Flows," AIAA-98-2780

10. Riggins, D.W. and Vitt, P.H., "Vortex Generation and Mixing in Three-Dimensional Supersonic Combustors," Journal of Propulsion and Power, Vol. 11, No. 3, 1995, pp. 419-426, May-June.

11. Lewis, D.P. and Schetz, J.A., "Tangential Injection from Overlaid Slots into a Supersonic Stream," Journal of Propulsion and Power, Vol. 13, No. 1, 1997, pp. 59-63, January-February.

12. Schetz, J.A., Billig, F.S., Favin, S., and Gilreath, H.E., “Effects of Pressure Mismatch on Slot Injection in a Supersonic Flow,” International Journal of Turbo and Jet Engines, Vol. 9, No. 2, 1992, pp. 135-146.

13. Tomioka, S., Jacobsen, L.S., and Schetz, J.A., “Sonic Injection from Diamond-Shaped Orifices into a Supersonic Crossflow,” Journal of Propulsion and Power, Vol. 19, No. 1, 2003, pp. 104-114, January-February.

14. Barber, M.J., Schetz, J.A., and Roe, L.A., “Normal Sonic Helium Injection Through a Wedge-Shaped Orifice into a Supersonic Flow,” Journal of Propulsion and Power, Vol. 13, No. 2, 1997, pp. 257-263, March-April.

15. Schetz, J.A., “Interaction Shock Shape for Transverse Injection,” Journal of Spacecraft and Rockets, Vol.7, No. 2, pp. 143-149, February 1970.

16. Fuller, E.J., Mays, R.B., Thomas, R.H., and Schetz, J.A., “Mixing Studies of Helium in Air at Mach 6,” AIAA Paper 91-2268, June, 1991.

17. McClinton, C.R., “The effect of Injection Angle on the interaction Between Sonic Secondary Jets and a Supersonic Freestream,” NASA TND-6669, February 1972.

18. Rogers, R.C., “A study of the Mixing of Hydrogen Injected Normal to a Supersonic Airstream,” NASA TN L-7386, Langley Research Center, March 1971.

19. Jacobsen, L.J., Schetz, J.A., Gallimore, S.D., and O’Brian, W.F., “Mixing enhancement by Jet Swirl in a Multiport Injector Array in Supersonic Flow,” FEDSM99-7448, July 1999

20. Kraus, D. K., and Cutler, A. D., “Mixing of Swirling Jets in a Supersonic Duct Flow,” Journal of Propulsion and Power, Vol. 12, No. 1, 1996, pp. 170-177, January-February.

21. Cutler, A.D., and Johnson C. H., “The Use of swirling Jet Pairs to Provide Rapid Fuel Penetration in Scramjet Combustors,” AIAA Paper 95-0099.

22. Schetz, J.A., “Injection and Mixing in a Turbulent Flow,” AIAA, New York, New York, 1980.

23. Povinelli, L.A., and Ehlers, R.C., “Swirling Base Injection for Supersonic Combustion Ramjets,” AIAA Journal, Vol. 10 No. 9, pp. 1243-1244, September, 1972.

24. Schetz, J.A., and Swanson R.C., “Turbulent jet Mixing at High Supersonic Speeds,” Vol.21, pp. 166-173,1973.

25. Schetz, J.A., Thomas, R.H., and Billig, F.S., “Mixing of Transverse Jets and Wall Jets in Supersonic Flow,” IUTAM Symposium on Separated Flows and Jets, Novosibirsk, July 1990.

26. Marzouk, Y.M., and Ghoniem, A.F., “Mechanism of Streamwise Vorticity Formation in Transverse Jets,” AIAA Aerospace Sciences Meeting and Exhibit, 40th, Reno, NV, AIAA 2002-1063, January, 2002.

27. Ng, W.F., Kwok, F.T., and Ninnemann, T.A., “A Concentration Probe for the Study of Mixing in Supersonic Shear Flows,” AIAA paper 89-2459, July 1989.

Appendix A

A.1 Helium Concentration Algorithms

```
clear
%This program calls the function which determines the helium concentration for each
point

% insert the pressures measured by the pressure transducer in the concentration probe
% collumns are the vertical traverse positions and rows are the horizontal stations
P_ = [];

% insert the voltages measured by the hotwire anemometer in the concentration probe
% collumns are the vertical traverse positions and rows are the horizontal stations
V_ = [];

% insert the temperatures measured by the thermocoupler in the concentration probe
% collumns are the vertical traverse positions and rows are the horizontal stations
T_ = [];


[j,w] = size(V_);
X_=0;
for h = 1:w,
for i = 1:j,
   [X,Xm] = concentration(V_(i,h),P_(i,h),T_(i,h));
   X_(i,h) = X;
   Xm_(i,h) = Xm;
end
end

%X_ is the mole fraction and XM_ is the mass fraction
X_
Xm_
Xm_ =
[Xm_(:,1);Xm_(:,2);Xm_(:,3);Xm_(:,4);Xm_(:,5);Xm_(:,6);Xm_(:,7);Xm_(:,8);Xm_(:,9)
;Xm_(:,10);Xm_(:,11);Xm_(:,12);Xm_(:,13)]
```

```
function [X,Xm] = concentration(V,Pt,Tt)

% V is the voltage of the hotwire
Pt = Pt.*6895;
% Pt is the total Pressure in Pa
Tt = Tt +273;
% Tt is the total temperature in K

Tw = 200+273;
% Tw is the hotwire operational temperature in K
Rw = 8.9;
% Rw is the hotwire operational resistance in Ohms
Rs = 20;
%Rs is the bridge resistence in ohms
Ath = 3.167e-7;
% Ath is the throat area in m^2
Ahf = 1.14e-5;
% Ahf is the calibration chamber area at the sampling plane in m^2
d = 50.8e-6;
% d is the hotwire diameter in m
l = .00102;
% active length of hotwire in m
Mair = 28.97;
% Mair is the molar mass of air in kg/kMol
Mhe = 4.0026;
% Mhe is the molar mass of helium in kg/kMol

X1=[0:.1:1];

a = [1.8872
    0.2799
    0.1630
    0.0937
    0.0626
    0.0434
    0.0402
    0.0419
    0.0524
    0.0628
    1.4905];

b = [0.2875
    0.3862
    0.4902
    0.6141
```

```
   0.7031
   0.7780
   0.7594
   0.6953
   0.5510
   0.4160
   0.2851];

V1=0;
c=0;
while max(V1) <= V & c <= 10,
   c=c+1;
   M = (1-X1(c))*Mair + X1(c)*Mhe;
   % M is the molar mass of the mixture in kg/kMol
   Xmhe = X1(c).*Mhe./M;
   % Xmhe is the mass fraction of helium
   Xmair = (1-X1(c)).*Mair./M;
   Rgas = 8314/M;
   % Rgas is the gas constant of the mixture J/kg K
   Cpair = (28110 + 1.967.*Tt + (4.802e-3).*(Tt.^2) - (1.966e-7).*(Tt.^3))/Mair;
   % Cpair is the specific heat of air at temperature Tt in J/kg K
   Cphe = 5192.6;
   % Cphe is the specific heat of helium in J/kg K
   Cp = Xmair.*Cpair + Xmhe.*Cphe;
   % Cp is the specific heat of the mixture in J/kg K
   gama = Cp./(Cp-Rgas);
   % gama is the ratio of specific heats of the mixture
   mdot = Pt.*Ath.*(((gama./(Rgas.*Tt)).*((2./(gama+1)).^((gama+1)./(gama-
1)))).^(1/2));
   % mdot is the mass flow rate
   rhov = mdot./Ahf;
   % rhov is the density times velocity at the sensor plane in kg/m^2 s
   %gamma = gama(1)
   %AoverAstar = Ahf/Ath
   %ToverTt = input('use the applet with gamma and AoverAstar to determine T/To at
the hotwire: ');
   %T = ToverTt.*Tt;
   T=Tt;
   %T is the temperature at the sensor plane in K
   muair = -1.31554e-6 + (9.53265e-8).*T - (1.50660e-10).*(T.^2) + (2.41737e-
13).*(T.^3) - (2.58576e-16).*(T.^4) + (1.26849e-19).*(T.^5);
   %muair is the visciosity of air at temperature T in kg/m s
   muhe = -4.56080e-6 + (2.05152e-7).*T - (8.89707e-10).*(T.^2) + (2.41714e-
12).*(T.^3) - (3.20720e-15).*(T.^4) + (1.63060e-18).*(T.^5);
   %muhe is the visciosity of helium at temperature T in kg/m s
   kair = 1.61344e-4 + (8.89970e-5).*T + (3.85599e-8).*(T.^2) - (2.39332e-10).*(T.^3) +
```

```
(3.48891e-13).*(T.^4) - (1.84858e-16).*(T.^5);
   % kair is the thermal conductivity of air at temperature, T in W m/K
   khe = 4.33185e-2 + (1.23854e-4).*T + (2.77149e-6).*(T.^2) - (1.11774e-8).*(T.^3) +
(1.81601e-11).*(T.^4) - (1.03892e-14).*(T.^5);
   % khe is the thermal conductivity of helium at temperature, T in W m/K
   Zairhe = (1 +
((Mhe/Mair)^(1/4)).*((muair./muhe).^(1/2)))./((4/sqrt(2)).*((1+(Mair./Mhe)).^(1/2)));
   Zheair = (1 +
((Mair/Mhe)^(1/4)).*((muhe./muair).^(1/2)))./((4/sqrt(2)).*((1+(Mhe./Mair)).^(1/2)));
   if X1(c) == 0,
      mu = muair;
      k=kair;
   elseif X1(c) == 1,
      mu=muhe;
      k=khe;
   else
      mu = (muair./(1+Zairhe.*((1-X1(c))./X1(c))))+(muhe./(1+Zheair.*(X1(c)./(1-
X1(c)))));
      % mu is the viscocity of the mixture at the given concentration for each temperature
Tt in kg/m s
      k = ( ((1-X1(c)).*kair+X1(c).*khe+kair.*khe)./( ((1-
X1(c)).*(khe.^(1/2))+X1(c).*(kair.^(1/2))).^2 ) )./2;
      % k is the thermal conductivity of the mixture at the given concentration in W m/K
   end
   %Reynolds Number
   Re = rhov.*d./mu;
   V1(c) = sqrt((((Rw+Rs)^2)/Rw)*pi*l*k*a(c)*(Re^b(c))*(Tw-T));
end
if c == 1,
   X_1 = 0;
   V_1 = 0;
else
   X_1 = X1(c-1);
   V_1 = V1(c-1);
end
X_2 = X1(c);
V_2 = V1(c);
X = ((X_2-X_1)/(V_2-V_1))*(V-V_1) + X_1;
M = (1-X)*Mair + X*Mhe;
Xm = X.*Mhe./M;
```

A.2 Aero-thermodynamic Algorithms

```
clear all
%This program determines the local total pressure and Mach number

% insert the pressures measured by the cone static pressure probe
% collumns are the vertical traverse positions and rows are the horizontal stations
P = [];

% insert the pressures measured by the Pitot pressure probe
% collumns are the vertical traverse positions and rows are the horizontal stations
Pt2 = [];

P=P./Pt2;
x = P-P;
M=P-P;
i=0;
j=0;
k=[size(P)]
for i = 1:k(1),
   for j = 1:k(2),
      x(i,j) = P(i,j);
      % power fit to the numerical solution of Tayler-Mccoll and normal shocj
      M(i,j) = 0.6767*x(i,j)^-0.735;
      Pt(i,j) = Pt2(i,j)./((((6.*M(i,j).^2)/(M(i,j).^2+5)).^3.5)*((6./(7.*M(i,j).^2-1)).^2.5));
   end
end
% M is Mach number and Pt is local mach number
M_=M
Pt_=Pt
M_=[M_(:,1);M_(:,2);M_(:,3);M_(:,4);M_(:,5);M_(:,6);M_(:,7);M_(:,8);M_(:,9);M_(:,10
);M_(:,11);M_(:,12);M_(:,12)]
Pt_=[Pt_(:,1);Pt_(:,2);Pt_(:,3);Pt_(:,4);Pt_(:,5);Pt_(:,6);Pt_(:,7);Pt_(:,8);Pt_(:,9);Pt_(:,10);
Pt_(:,11);Pt_(:,12);Pt_(:,13)]
```

A.3 Concentration Probe Calibration Results

Figure A.1 shows the calibration curves for the concentration probe the curves go from 0% helium to 100% helium from the bottom of the plot to the top. The circles represent the values measured in the calibration and the lines represent the curves fit to these values.

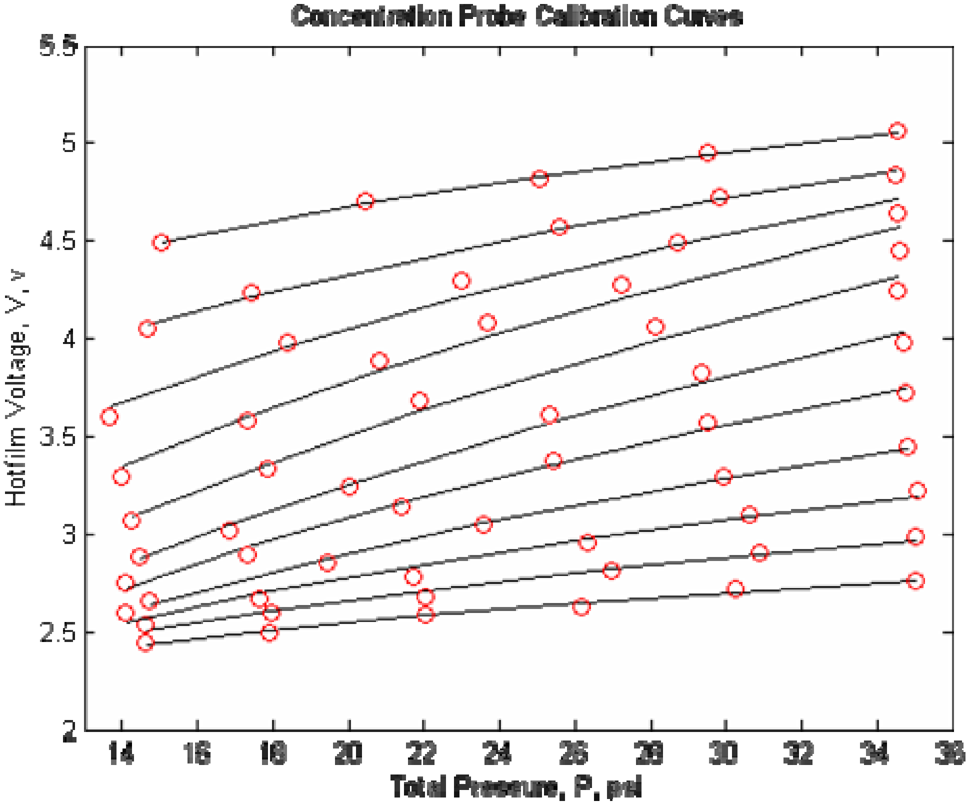

Figure A.1: Concentration Calibration Results

Vita

Peter Michael Grossman was born on December 18, 1981 in Greenville, North Carolina and grew up in Chapel Hill, North Carolina. After High School, he entered Virginia Tech in 2000 where he pursued his Bachelors degree followed by his Masters degree. During his undergraduate time, he spent the spring semester of 2004 at the University of Glasgow as part of a study abroad program.